The final publication is available at

https://doi.org/10.1038/s41929-021-00592-3

Additional Information

Regioirregular and catalytic Mizoroki–Heck reactions

Francisco Garnes–Portolés,[†,◊] Rossella Greco,[†,◊] Judit Oliver–Meseguer,[†] Jorge Castellanos–Soriano,[§] M. Consuelo Jiménez,[§] Miguel López–Haro,[‡] Juan Carlos Hernández–Garrido,[‡] Mercedes Boronat,[†] Raúl Pérez–Ruiz*[,§] and Antonio Leyva–Pérez.*[,†]

[†] Instituto de Tecnología Química (UPV–CSIC), Universitat Politècnica de València–Consejo Superior de Investigaciones Científicas, Avda. de los Naranjos s/n, 46022 Valencia, Spain.

[§] Departamento de Química, Universitat Politècnica de València, Camino de Vera s/n, 46022 Valencia, Spain.

[‡] Departamento de Ciencia de los Materiales e Ingeniería Metalúrgica y Química Inorgánica, Facultad de Ciencias, Universidad de Cádiz, Campus Universitario Puerto Real, 11510 Puerto Real, Cádiz, Spain.

[◊] These authors equally contributed to the work

Corresponding authors´ emails: raupreru@qim.upv.es, anleyva@itq.upv.es.

ABSTRACT: **The palladium–catalysed cross–coupling reaction between alkenes and aryl halides (Mizoroki–Heck reaction) is a powerful methodology to construct new carbon–carbon bonds[1]. However, the success of this reaction is in part hampered by an extremely marked regioselectivity on the double bond, which dictates that electron–poor alkenes react exclusively on the *beta* carbon[2]. Here, we show that ligand–free, few–atom palladium clusters in solution catalyse the α–selective *intra*molecular Mizoroki–Heck coupling of iodoaryl cinnamates, and mechanistic studies support the formation of a sterically–encumbered cinnamate–palladium cluster intermediate. Following this rationale, the α–selective *inter*molecular coupling of aryl iodides with styrenes is also achieved with palladium clusters encapsulated within fine–tuned and sterically–restricted zeolite cavities, to produce 1,1–bisarylethylenes which are further engaged with aryl halides by a metal–free photoredox catalysed coupling. These ligand–free methodologies significantly expand the chemical space of the Mizoroki–Heck coupling.**

INTRODUCTION.

The regioselectivity of the intra– and intermolecular Mizoroki–Heck coupling[3] is basically dictated by the chemical nature of the alkene coupling partner. Electron–poor alkenes, perhaps the most used starting alkenes for the reaction (i.e. acrylates and styrenes), give *E*–1,2–alkenes (β coupling) as major reaction products, since the neutrally charged Pd intermediate inserts the alkene in such a way that the electron withdrawing group (EWG) points away from the coupling position. This stereochemical outcome, shown in Figures 1a and 1b, is switched in the cationic mechanism, where alkenes with electron donor groups (EDG), i.e. vinyl ethers, give the 1,1–alkene product (α coupling)[4]. Coherently, neutral alkenes, i.e. alkyl alkenes, give mixtures of β and α products, and it is difficult to find in the open literature any example which clearly contradicts the regioselective rules shown in Figure

42 1b. Reported alternatives consist in the use of sterically encumbered stoichiometric Pd

43 complexes[5] or aryl pseudohalides, such as aryl sulfonates[6], triflates[7], carboxylates[8] and

44 diazocompounds[9], which also trigger a cationic pathway to give the α product regardless of

45 the alkene partner used. While these strategies are remarkable, the complex Pd catalyst and

46 the aryl pseudo–halide are much more laborious to prepare and expensive than typical

47 palladium catalysts and aryl halides for conventional Mizoroki–Heck reactions. An additional

48 issue of the intermolecular coupling is the lack of reactivity of polysubstituted alkenes, as

49 shown in Figure 1c, which is severely restricted by the prohibitive steric hindrance generated

50 during alkene insertion into nearly planar alkene–Pd intermediates[10]. Together, these

51 limitations explain why more than the half of the theoretical possible couplings are, in

52 principle, not feasible yet in reasonable yields, as illustrated in Figure 1d, and why the

53 Mizoroki–Heck reaction is still underrepresented in industrial applications compared to other

54 reactions, since, for instance, the synthesis of cinnamates can also be performed in industry by

55 aldol–type condensations of the corresponding aldehydes and esters[11].Apart from electronics,

56 regioselectivity also follows steric restrictions based on the strict accommodation of the

57 sterically encumbered substrate around the catalytic Pd site. As a result, *exo–* and *endo–*

58 products in the intramolecular coupling are formed depending if the final product is a 5–8 or a

59 9– or higher carbon–atom member ring, respectively[12]. To our knowledge, both the electronic

60 and the steric regioselectivity pattern have not been put in conflict during an intramolecular

61 Mizoroki–Heck reaction[13] (see also Supplementary Discussion). Here we show the α

62 coupling of electron poor alkenes with aryl iodides, in both intra– and intermolecular

63 versions, and also the coupling of polyarylsubstituted alkenes with aryl bromides and one aryl

64 chloride, as shown in Figure 1e. The former is based on the use of sterically encumbered but

65 ligand–free Pd cluster catalysts, where the Pd intermediate is enclosed by either the substrate

66 itself (intramolecular) or by a zeolite cavity (intermolecular, see Figure 1B), and the latter

67 relies on a metal–free visible–light induced photoredox catalysed system, which circumvents

68 clashed planar Pd complexes (see Figure 1c).

69

70 **RESULTS**

71 **α–Selective *intra*molecular Mizoroki–Heck coupling..**

72 Table 1 shows the results for the intramolecular Mizoroki–Heck coupling of aryl *o*–iodide–

73 substituted cinnamic ester **1a**[14], which according to the steric rules should give the α coupling

74 product **2a** but according to the electronic rules should give the β coupling product **3a**.

75 Different representative Pd complex catalysts[15] (2 mol%) for the Mizoroki–Heck reaction

76 gave low yields of product **2a**, under optimal reaction conditions for their respective catalytic

77 activity (entries 1–15), however, in–situ generated catalytic ligand–free ultrasmall $Pd_{3–4}$

78 clusters[16] gave significant amounts of the α product **2a** (entries 16–20), up to a 69% yield by

79 gas chromatography (GC, as a 4:1 mixture of *E* and *Z* isomers, see Supplementary Figure 1)

80 and with an isolated yield after column chromatography of 52% for the α–*E* product **2a** and

81 <10% for the β coupling product **3a**. The cinnamic ester **1aa**, with an additional carbon atom

82 in the alkyl chain, was also prepared and tested as a starting material for the coupling, and the

83 result showed that the α coupling product, the unfavored seven–member ring ε–lactones **2aa**

84 and **2ab** were formed in 55% isolated yield, without any trace of β coupling product **3aa**

85 (entry 21, see also Supplementary Figure 1). This last result confirms the preferential

86 formation of the α–coupling product beyond the intrinsic stability of δ– and ζ– *vs.* ε–lactones.

87   Figure 2 shows that cinnamates **1a–m** cyclise in the presence of ligand–free $Pd_{3–4}$ catalysts

88 to give the corresponding α coupled, exo–benzylenyl δ–lactones **2a–m** in excellent yields and

89 reasonable stereoselectivity, with the *E* isomer as the major product. These results strongly

90 support that *exo* regioselectivity takes control and violate the long accepted β–directing

4

91 electronic rules for the Mizoroki–Heck reaction in aryl iodide–substituted cinnamyl esters

92 **1a(a)–m**, with catalytic Pd$_{3-4}$ clusters, to intramolecularly couple the α carbon atom of the

93 electron–poor alkene to the aryl iodide, and give otherwise difficult to prepare *exo–*

94 benzylidene lactones **2a(a)–m**[17,18].

95 The highly conjugated structure of benzyl cinnamate esters **1a–z** did not invite, in a first

96 approach, to expect any intramolecular coupling (neither α nor β), since the carbon–iodide

97 and alkene reactive groups are far away to be accommodated by one Pd atom in the expected

98 quasi planar configuration. Indeed, density–functional theory (DFT) calculations show that

99 the reactive groups are indeed separated by more than 5   in the bowl shaped, most stable

100 configuration of pristine **1a** (Supplementary Figure 2 and Supplementary Table 1), and that

101 this distance remains larger than 4.6   after oxidative addition of one single Pd atom (**1a–**

102 **Pd$_1$**) and two Pd atoms (**1a–Pd$_2$**), regardless the initial configuration of pristine **1a**

103 (Supplementary Figure 3 and Supplementary Table 1). In all these systems the Pd atoms

104 coordinate to the *sp^3* oxygen atom of the ester group, and the organometallic structure is

105 nearly planar. In contrast, the most stable coordination modes of **1a** with Pd$_3$ and Pd$_4$ clusters

106 involve the *sp^2* oxygen atom of the carbonyl group (structures labelled A in Figure 3a and

107 Supplementary Figure 4) or the C=C bond (structures labelled B in Figure 3a and

108 Supplementary Figure 4), with the ester linked structures C and D being clearly less favored.

109 This change in the preferred coordinating mode is a consequence of both the fluxionality of

110 the Pd$_3$ and Pd$_4$ clusters, which allows to spatially reach further atoms on the linear molecule

111 **1a**, and of their electronic distribution, with an empty LUMO orbital spread over the whole

112 cluster which allows to form multiple Pd–C and Pd–O bonds (Figure 3b). In the B-type

113 coordination mode the reactant groups are placed near enough for the coupling (see optimized

114 distances in Supplementary Table 1), with the Pd$_4$–I–B structure being particularly favorable

115 (the optimized C–Cα and C–Cβ distances in Pd$_4$–I–B are 3.03   and 3.66   , respectively).

116   Starting from B–type structures, the transition states and products for the α and β

117   intramolecular couplings in **1a** were calculated, and the results shown in Figures 3c and

118   Supplementary Figures 5–6. The optimized length of the C-C bond being formed is similar,

119   2   in all cases (see Supplementary Table 2), but the different number of additional

120   interactions that can be formed between the Pd cluster and the organic skeleton of **1a** leads to

121   differences in activation energies as large as 24 kcal·mol^{-1}. According to the DFT results, the

122   α–coupling in **1a** is energetically affordable in Pd$_4$–I model, with an intrinsic activation

123   energy of 19.7 kcal·mol^{-1} (Figure 3d), while the β-coupling requires surpassing barriers larger

124   than 34 kcal·mol^{-1} in all cases considered. Although we have not calculated the activation

125   energies for all the steps of the mechanism, activation barriers for the alkene-insertion step in

126   the metal cluster catalysed regular coupling are around 30 kcal·mol^{-1}, clearly higher than

127   those obtained for the oxidative addition of the aryl iodide (1–2 kcal·mol^{-1}) and the beta–

128   elimination steps (7 kcal·mol^{-1})[19]. For the regio–irregular coupling here, the activation

129   energies obtained for the alkene insertion steps on the equivalent Pd$_3$–I catalyst model are 34–

130   38 kcal·mol^{-1}, suggesting that the rate–determining step (rds) might also be the alkene–

131   insertion, as in a typical Heck reaction.

132   The fact that iodine, once bound to Pd, helps during the catalysis, is clearly supported by the

133   calculations and deserves a separate study. A preliminary experiment was carried out with the

134   commercially available catalyst [Pd(μ-–I)(Pt–Bu$_3$)]$_2$, where the Pd atom is connected to two

135   bridging–μ–I atoms, and which has been reported to be active for the intermolecular

136   Mizoroki–Heck coupling[20], and the results show that this iodine–containing Pd catalyst is

137   much more active than Pd(OAc)$_2$ and close to the activity of Pd$_4$–MOF clusters[21] in o–xylene

138   (Supplementary Figure 7).

139   In order to directly visualize the Pd clusters, high-resolution high–angle annular dark–field

140   scanning transmission electron microscopy (HR HAADF–STEM) measurements of the DMF

141 solution were performed. Notice the difficulties associated to directly image the clusters in

142 solution, without any support. The results in Figure 3c shows the main Pd species visible in

143 solution correspond to aggregations between 0.5–0.8 nm in size, which corresponds to Pd

144 clusters of 4±1 atoms. Computational simulations confirm this size for the Pd clusters in

145 solution (Supplementary Figure 8), which are in good agreement with the previously observed

146 size for these Pd clusters[16,19] and confirm the experimental and computational evidences

147 obtained here during the regio–irregular Mizoroki–Heck reaction.

148 **- Kinetic and reactivity studies: proposal of a plausible mechanism for the regio–**

149 **irregular intramolecular coupling.**

150 Kinetic measurements in *N,N*–dimethylacetamide (DMAc) instead of DMF solvent (in order

151 to increase the reaction temperature up to 170 ºC) show that the activation energy for the

152 intramolecular coupling of **1a** is 21 KJ·mol^{-1} but, in contrast, the activation energy for the

153 intermolecular coupling of iodobenzene **5a** with benzyl cinnamyl ester **1n** is 98 KJ·mol^{-1}

154 (Supplementary Figure 9). Thus, the measured activation energy for the α–selective

155 intramolecular coupling is nearly four times lower, under the same experimental conditions,

156 than the β–selective intermolecular coupling. Additional kinetic measurements with different

157 *p*–substituted aryl *o*–iodide cinnamyl esters give a ρ= +1.0(5) in the Hammett plot

158 (Supplementary Figure 10), which clearly indicates that a negative charge is located in the β

159 carbon atom of the alkene during the α–selective coupling, in other words, that Pd insertion

160 exerts an umpolung of the carbon-carbon bond. Complementary, electron–deficient aryl

161 iodides react more easily than the electron–rich counterparts or aryl bromides, which fits the

162 expected order of reactivity for the oxidative addition step. The experimental rate equation

163 obtained with different concentrations of **1a**, catalyst and base, is $v_0= k_{exp}[Pd_{3-4}][1a][Base]$

164 (1) (Supplementary Figure 11), with all the reagents taking part in the rate determining step

165 (rds) of the coupling, which supports a late transition state where β hydride elimination is

166 implicated[19]. The computational and experimental results, together, strongly support that the

167 intramolecular Mizoroki–Heck coupling of **1a** operates with catalytic Pd$_{3-4}$ clusters under the

168 canonical steps of the coupling, i.e. oxidative addition – alkene insertion – β–hydride

169 elimination, to intramolecularly accommodate the aryl iodide and the alkene for the α

170 coupling on the basis of steric requirements, regardless electronics, and with a significant

171 umpolung of the alkene.

172 α–Selective *inter*molecular Mizoroki–Heck coupling.

173 Taking into account that a bowl–shaped Pd$_{3-4}$ cluster–substrate intermediate, of

174 approximately 1 nm diameter size, enables the intramolecular α coupling of the very electron

175 deficient alkenes **1a(a)–m** in solution, we wondered if this catalytic cage could be mimicked

176 by Pd clusters enclosed within the cavities of a porous macromolecule of similar size[21], in

177 order to perform the intermolecular Mizoroki–Heck coupling. This molecular confinement

178 will artificially play the role of the cinnamyl ester carbon chain skeleton in **1a**, to embed the

179 Pd$_{3-4}$ cluster and enable reactant activation and coupling. Of course, the catalytic design

180 requires an exquisite control of the cavity size and also the accommodation of a proximal

181 basic site, since the concomitant diffusion of an external base within the catalytic site of a

182 rigid macromolecule may turn out difficult. Here, we envisioned the use of basic zeolites as

183 both support for Pd and base for the α–selective intermolecular Mizoroki–Heck reaction, an

184 approach that radically circumvents the use of ligands, the only candidates proposed so far

185 with computational calculations to theoretically switch the outcome of electron–deficient

186 alkene couplings[22,23] (see also Supplementary Discussion).

187 H$^+$ or Na$^+$–exchanged Y and X zeolites are able to accommodate Pd clusters within the

188 supercages and catalyse the nominal Mizoroki–Heck reaction with an external base, to give

189 exclusively the classical β intermolecular product[24,25]. However, , the FAU supercage shows

190 the appropriate dimensions to simulate the Pd intermediate involved in the α selective

191   Mizoroki–Heck coupling of **1a** and also hosts counterbalancing cations to tune not only the

192   void space but also the basicity of the zeolite [three cations in zeolite Y (Si/Al= 2.5) and ten

193   cations in zeolite X (Si/Al= 1.2)]. Thus, it may occur that exchanging the extra–framework

194   Na^+ cations (ionic radius 1.0 Å) by bigger ones such as K^+ (ionic radius 1.5 Å) or Cs^+ (ionic

195   radius 1.7 Å) will build up a suitable Pd catalyst to switch the selectivity of the Mizoroki–

196   Heck reaction from the β to α product[26]. Indeed, Na^+ locates in the small rings of the zeolite

197   cavity walls while Cs^+ locates in the bigger supercages, which increases the steric hindrance

198   provoked by the latter in the reaction site.

199   Figure 4a illustrates this hypothesis, where the size and the number of the extra–framework

200   cations modulate the size and basicity of the Pd–containing supercages. A rapid calculation

201   confirms that every exchange of Na^+ by Cs^+ increases the occupied space by 7 $Å^3$ at least,

202   approximately 5% of the void volume. To test the hypothesis, Pd^{2+} was introduced in basic

203   zeolites[27] (see methods) And the resulting Pd^{2+}–$M^+(N)$–zeolites (M= Na, K or Cs; N= 1–3

204   exchanges; zeolites Y or X) were then calcined at 400 ºC under air to trigger the formation of

205   Pd clusters (Pd–$M^+(N)$–zeolite), except for CsX zeolites, where a rapid formation of black Pd

206   was observed at temperatures >200 ºC. This result showcases the high electron density of the

207   CsX zeolite, provoked by the hosted Cs^+ cations, and indeed, a simple drying at 100 ºC in an

208   oven is enough to trigger the Pd cluster formation[28].

209   The catalytic solids were analyzed by powder X–ray diffraction (PXRD), thermogravimetry

210   (TG), Brunauer–Emmett–Teller surface area measurements (BET) and infrared spectroscopy

211   (IR, Supplementary Figures 12–15), which confirmed the integrity of the zeolite framework

212   after incorporation of Pd^{2+} and Cs^+, and the expected decrease of internal volume. Diffuse

213   reflectance ultraviolet–visible spectrophotometry (DR–UVvis, Supplementary Figure 16)

214   shows the typical absorption bands for confined species of PdO at 240-300 nm, and Cs_{3d} and

215   Pd_{3d} X–ray photoelectron spectroscopy (XPS, Supplementary Figure 17) shows well

216   separated spin-orbit components for Cs^+ and Pd^{2+} (Δ=14 and 5 eV, respectively), compatible

217   with the hydroxide and oxide species, and without apparent formation of Pd(0) in the

218   uncalcined samples[29]. These results support the successful incorporation of Pd^{2+} within the

219   zeolite framework. Figure 4b shows the extended X–ray absorption fine structure (EXAFS)

220   and X–ray absorption near edge structure (XANES) spectra of uncalcined and used Pd–

221   Cs(3)X. The k^3–weighted (phase uncorrected) Fourier Transform spectrum shows that the Pd

222   atoms in uncalcined Pd–CsX have the first coordination shell in the same position (around 1.5

223   Å) of PdO, characteristic of square planar compounds. Besides, the contribution of higher

224   coordination shells is very low, in accordance with the potential formation of tiny PdO

225   clusters within the zeolite. This contribution disappears after reaction to give a Pd–Pd first

226   shell contribution, also observed in the Pd foil sample, but with many lesser contributions

227   after 3 Å. These results are in good agreement with the expected reduction of Pd during the

228   catalytic cycle and the formation of very small Pd clusters confined within the zeolite

229   nanostructure, which according to the fitting corresponds to a central Pd atom surrounded of 4

230   Pd atoms (Supplementary Table 3)[30]. The lower amplitude of the EXAFS oscillation after

231   reaction is also indicative of the formation of ultrasmall Pd clusters. The XANES Pd K–edge

232   confirms that the Pd atoms in fresh Pd–Cs(3)X are in oxidized form (24368 eV) and became

233   reduced after reaction (24385 eV). Aberration–corrected high–resolution transmission

234   electron microscopy measurements were then attempted, despite the high atomic weight of

235   Cs^+ severely hampers the correct visualization of the Pd atoms within the zeolite[31–34]. Figure

236   4c shows that the majority of Pd ensembles observed by electron microscopy have a size

237   around 0.6–0.8 nm embedded within the zeolite channels (see Methods and Supplementary

238   Figure 8 for details), and this size nicely fits with the experimental size observed above for

239   the catalytically active clusters in solution. Computational simulations agree satisfactorily

240   with this size, thus one can say that Pd clusters between 3 and 5 atomsare the catalytic active

241   species for the regio–irregular Mizoroki–Heck reaction both in solution and in the zeolite.

242   While it is true that a mixture of single Pd atoms and ultrasmall clusters reside together within

243   the zeolite (Supplementary Figure 8,)[31], the results in solution and the fact that the generation

244   of Pd clusters inside small zeolite frameworks is in principle favored under calcination

245   conditions[32,33], make Pd clusters as the plausible catalytic species here. Table 2 shows the

246   catalytic results for the Mizoroki–Heck coupling of iodobenzene **5a** and styrene **6a** with the

247   bifunctional Pd–base zeolites, without addition of any external base. Gratifyingly, the

248   bifunctional solids give the α coupling product **7a** when the proper basicity and steric

249   hindrance is achieved, starting with K^+–X zeolites (compare entries 1–12) and peaking up

250   with Pd–Cs(3)X, to give a 57% isolated yield of **7a** after 2 h reaction time (entries 13–16).

251   Remarkably, a Pd–Cs(3)X sample prepared >15 years ago, with $PdCl_2$ instead of K_2PdCl_4,

252   showed a similar catalytic activity and selectivity. A new sample of Pd–Cs(3)X with 5 wt%

253   Pd gives a somewhat higher isolated yield of **7a** (70%, entry 17), and mesitylene was used as

254   a solvent, since DMF or DMAc gave exclusively the β product **8a**[24] after leaching of Pd. The

255   α selectivity rises with the basicity and steric hindrance increase within the zeolite and, in

256   order to decouple these two factors, the basicity of Pd–Cs(3)X was further increased after

257   generating more Cs_2O particles inside the zeolite by addition of a base Cs^+ solution, in zeolite

258   positions which do not modify the steric hindrance of the supercage[35]. The result shows that

259   this superbasic zeolite is neither more active nor more α–selective for the coupling (entry 18).

260   Additionally, a Pd–Na(Ge)X zeolite[36], containing Ge instead of Si on the framework, gave

261   very low amounts (<5%) of **7a**, even though GeX zeolite shows a much higher framework

262   electron density than the parent (Si)X zeolite due to the softer nature of Ge compared to Si.

263   These results support that not only the basicity but also the steric hindrance exerted by the Cs^+

264   atoms on the Pd cluster in the supercage plays a decisive role in the α–selective reaction and,

265   indeed, a hierarchical Pd–CsX zeolite[37], with much lower basicity than the microporous 3D

266   standard one but with a higher internal volume and better diffusivity (see Supplementary

267   Figure 14), still gave a significant amount of **7a** (entry 19).

268   Figure 5a shows that both the conversion and the α–selectivity linearly drop with the increase

269   in kinetic radius of the different para–substituted iodobenzenes, which is a direct

270   measurement of the ability of the substrate to be accommodated into the Pd–loaded zeolite

271   supercage. In contrast, iodobenzene electronics are randomly distributed in any Hammett plot

272   correlation, thus substrate electronics do not directly control reactivity within the zeolite

273   cavity (Supplementary Figure 18). These results strongly support that Pd cluster catalysts in

274   combination with base zeolites generate the suitable steric spatial arrangement for an α–

275   selective coupling. The hierarchical zeolite significantly improves the coupling of the more

276   hindered *p-tert*-butyl-iodobenzene compared to the regular zeolite, which confirms the steric

277   requirements imposed by the base zeolite (Supplementary Figure 19). Kinetic measurements

278   for the coupling of **5a** with **6a** catalysed by Pd–Cs(3)X, at different concentrations of

279   reactants and solid catalyst (Supplementary Figure 20), give the rate equation

280   v_0=k$_{exp}$[zeolite][**5a**][**6a**] (2). The change of iodobenzene **5a** to bromo– and chlorobenzene

281   shows the typical decrease in reactivity for the Mizoroki–Heck coupling (the reactivity of

282   each halide is reduced by ca. one order of magnitude, Supplementary Figure 21), however,

283   still preserving a similar α–selectivity for **7a**. The kinetic isotopic effect obtained in parallel

284   experiments with alkenes **6a** and **6a–d^2** (Supplementary Figure 22) shows a KIE= 1.3(4).

285   These results point to a late transition state during the α–selective coupling, where not only

286   iodobenzene **5a** and Pd–Cs(3)X, but also the alkene **6a**, are implicated in the rate–determining

287   step (rds) of the coupling, as it occurs above for the intramolecular coupling. The kinetic

288   profile of the reaction shows a rapid poisoning of the catalyst, since nearly the 90% of the

289   activity occurs in the first five minutes of reaction (see for instance Supplementary Figure

290   22). Besides, a small but detectable induction time of 1–2 min can be seen. Since the reaction

291   is carried out by adding **5a** on the mesitylene mixture containing **6a** and the solid catalyst at

292   175 ºC, experiments at different stirring rates were performed, in order to unveil a potential

293   diffusion control[38]. However, the results show that the reaction is not controlled by diffusion

294   (Supplementary Figure 23), neither for **5a** nor for sterically hindered *p-tert*-butyl-

295   iodobenzene. Tests with product **7a** (0.5 eq.) as an additional starting material

296   (Supplementary Figure 24) discards any self–poisoning of the coupling by the product but, in

297   contrast, a sample of Pd–Cs(3)X impregnated with an aqueous solution of CsI (1 eq. respect

298   to **5a**), the expected by–product of the reaction, showed a significant decrease of the overall

299   activity, but not of the selectivity (entry 20 in Table 2). These results indicate that the product

300   diffuses smoothly out but CsI is formed during reaction and blocks the catalyst pores, to stop

301   the reaction. Notice that the amount of basic sites is enough to complete the reaction, since the

302   simplified formula of the Cs-X zeolite, $Cs(AlSiO_2)$, gives us that the solid could contain up to

303   5 mmol of basic sites per gram (as a maximum), and here 200 mg of zeolite (1 mmol of basic

304   site) per 0.1 mmol of iodobenzene are employed (up to 10-fold excess). A CsI blockage is

305   reasonable considering the low polarity of the solvent, and the lack of metal leaching from

306   catalytic Pd–containing solids immersed in hot toluene derivative solutions[25–27]. If this is so,

307   washings of the used solid catalyst with an aqueous solution of Cs^+ ions, in order to remove

308   the barely adsorbed CsI species, should regenerate the basicity of the zeolite while keeping

309   the catalytic Pd clusters. Indeed, the used Pd–Cs(3)X catalyst recovered the full original

310   activity and selectivity after been washed at room temperature (entry 20). Regarding the

311   induction time, it was observed that the sequential addition of **5a** or **6a** after 2 min reaction

312   time, does not produce any change in the kinetic reaction profile. However, the induction time

313   is nearly undetectable under open reflux conditions rather than in sealed vials, and for the

314   former, a rapid exothermic burst can be visually appreciated when the coupling starts. We

315   tentatively associate the induction time, apart to the reduction of PdO to the Pd clusters, to the

316   removal of strongly adsorbed water within the zeolite, which clear the Pd catalyst and basic

317   sites for the reaction. Figure 5b shows that the catalytic system based on Pd–Cs(3)X can be

318   engineered to work in flow, in a rare example of continuous Mizoroki–Heck reaction[39]. Since

319   both the Pd catalyst and the inorganic base are contained within the solid, leaching does not

320   occur, and the catalytic solid can be easily activated after use by water washings. In this way,

321   pelletized Pd–Cs(3)X was introduced in a fixed–bed tubular reactor at 175 ºC and a solution

322   of **5a** and **6a** in mesitylene was passed through, to give a consistent yield and selectivity of **7a**

323   >50% for 1 h, after a stabilization period of 20 min. After reaction, an aqueous solution of

324   Cs_2CO_3 was passed through the reactor at 140 ºC in order to regenerate the solid catalyst, and

325   after drying the solid catalyst with a nitrogen stream at room temperature, the reaction

326   mixture was passed again to give **7a** in >40%, without any stabilizing period. A third use of

327   the catalyst was also fruitful, even though a loss in efficiency of the catalyst through the uses

328   could be observed, which may be due to uncomplete regeneration of the catalyst and some

329   leaching of Pd. Further studies are required here to achieve a complete continuous catalytic

330   system for the α–coupling, however, these results are promising towards the development of

331   such a solid–catalysed, in–flow system.

332   Figure 6 shows the results for the coupling of different iodobenzenes **5a–g** and styrenes **6a–o**

333   catalysed by Pd–Cs(3)X under optimized conditions, to give the α–coupling products **7a–x** in

334   good yields, up to 83%. A survey of the results reported in the literature for the same

335   couplings, with any other catalyst, and tested here by us with catalyst **4b**[15], give

336   systematically <10% of the β–products **8a–l** (the only exception for product **8c** which, in our

337   hands, is obtained in 13% at full conversion).

338   ***Inter*molecular metal-free organophotocatalytic Mizoroki–Heck coupling..**

339   The popularity of the Mizoroki–Heck coupling is in part due to a selective monoarylation of

340   the alkene, since the corresponding disubstituted alkene product does not further evolve to a

341 highly coupled product[40], despite a second coupling is electronically favored. As commented

342 above, steric effects during the Pd–alkene insertion step take control at this stage, hampering

343 the activation of disubstituted alkenes, particularly for aryl bromides. The ligand–free Pd–

344 catalysed system reported here somewhat alleviates this limitation, as shown in products **7m**

345 and **7t–v**, however, with still a very narrow window of activity, and only for iodobenzenes.

346 Assuming that the impeded insertion of sterically encumbered aromatic alkenes on the Pd

347 catalytic sites, severely restricts intermolecular Mizoroki–Heck couplings, the design of a

348 metal–free catalytic system was envisioned here, on the grounds that the acceptance of free

349 radicals is favored in polyaromatic alkenes[41]. This catalytic design would be particularly

350 effective in the activation of quaternary alkenyl carbon atoms, such as those in the 1,1–

351 diarylethylenes **7a–x** products synthesized in Figure 4b, since the diaryl–substituted benzylic

352 position naturally stabilizes a free radical[42].

353 Visible–light–driven construction of substituted triarylethylenes (TAEs) has been previously

354 studied[43,44], and with previously well–established optimal conditions in mind[45,46], aryl

355 bromides **9a–f** and 1,1–diphenyethylenes **7a,q,y,z** were put in the presence of catalytic

356 amounts of (4,4'–diiodo–bis(difluoroboron)1,2–bis((1H–pyrrol–2–yl)methylene)hydrazine

357 **BOPHY** (1% mol) and 9,10–diphenylanthracene **DPA** (10% mol) in an anaerobic

358 acetonitrile/dimethylacetamide (5/1 v/v) solution, and the mixture was submitted to visible

359 light irradiation with a laser pointer diode (λ_{exc} = 445 nm ± 10 nm, 2W, Supplementary Figure

360 25). Extended data figure 1 shows that TAEs **10a–o** are successfully obtained, in up to 80%

361 yield after 5 h reaction time, confirming that the adaptation of this photoredox catalytic

362 system to the desired Mizoroki–Heck coupling is immediate and symbiotic. To highlight here

363 is that similar conditions could be applied to aryl chloride **9f** as a starting material, forming

364 the desired product **10d**. *Ortho*–substituted aromatic rings are also tolerated, although

365 generally in lower yields (products **10e**, **10h**, **10m–o**) compared to the corresponding *para*–

15

366   substituted products (i.e. **10a** and **10f**), and *ortho* substitution seems to hamper the coupling

367   irrespectively if a metal catalyst is used or not, since it also occurs for Pd–catalysed regio–

368   irregular couplings (compares above substrates **7j** and **7k**, and **7f** and **7o**). Extended data

369   figure 2 (see also Supplementary Figures 26–31 and Supplementary Discussion) shows

370   experimental transient absorption spectroscopy (TAS) and quenching experiments, which

371   supports a plausible mechanism (Figure 2b). All the results, together, indicate a triplet fusion

372   upconversion (TFU, also named triplet–triplet annihilation) mechanism[47].

CONCLUSIONS

374   Regioirregular Mizoroki–Heck reactions of electron–deficient alkenes, including the Pd

375   cluster–catalysed α–selective intramolecular coupling of iodoaryl cinnamates, the Pd–CsX–

376   catalysed α–selective intermolecular coupling of aryl iodides and styrenes, and the

377   organophotocatalysed coupling of aryl bromides with polysubstitued ethylenes under visible

378   light, have been achieved in reasonable yields and good selectivity, to give access to *exo*–

379   benzylidene δ– and ε–lactones (14 examples, up to 99% yield), 1,1–bisarylethylenes (24

380   examples, up to 83% yield) and polyaromatic alkenes (12 examples, up to 80% yield),

381   respectively. These practical, cheap and industrially viable catalytic systems widely expand

382   the chemical space of the Mizoroki–Heck reaction, and pave the way for the design of ligand–

383   free Pd catalysts not only for the synthesis of alkenes but also of esters and polyaromatic

384   molecules[48], while preserving the activation of common aryl halides[49,50].

385

METHODS

387   **General preparation of basic zeolites and Pd^{2+} incorporation.** Commercially available Y

388   and X zeolites, in Na$^+$–form, were treated with an aqueous solution of K$^+$ or Cs$^+$ acetate, to

389   give the corresponding K$^+$– and Cs$^+$–zeolites (KY, CsY, KX and CsX). The extent of this first

390   exchange is typically 65% and 25% for K^+ and Cs^+, respectively, and two more consecutive

391   exchanges were carried out in order to increase the total cation exchange to 75% and 36% for

392   K^+ and Cs^+, respectively [K(3)Y,…]. The resulting solids were impregnated with an aqueous

393   solution of K_2PdCl_4 in methanol and left to evaporate to give 1 wt% Pd–loaded zeolites[27]. In

394   this way, no further cation exchange occurs, and the Pd is distributed along the zeolite

395   channels and cavities as Pd^{2+} without further counterbalancing of the zeolite basic sites, since

396   the Pd vehicle ($PdCl_4^{2-}$) is present as an anion.

397   **Preparation of PdCs(n)X.** In a round bottom flask equipped with a magnetic stir bar, 10 g of

398   NaX zeolite and 50 mL of a 1M solution of CsOAc were introduced. The mixture was placed

399   in a pre–heated oil bath and magnetically stirred at 80 °C for 8 h. After this time, the solid

400   was filtered under vacuum suction and washed with water, to give the CsX zeolite after

401   drying in an oven at 110 ºC for 16 h. This procedure is repeated once or twice to obtain

402   Cs(2)X and Cs(3)X zeolites, respectively. The solid obtained is impregnated with a 0.1M

403   solution of potassium tetrachloropalladate (II) in water (1.88 mL per 1 gram of zeolite), and

404   the mixture is dried in an oven at 60 ºC for 16 h to obtain Pd(1 wt%)–Cs(n)X. For Pd at 5

405   wt%, the amount of Pd precursor was increased five times in the impregnated solution.

406   α–**Selective intramolecular coupling of o–iodoaryl cinnamates.** In a 2 mL glass vial

407   equipped with a magnetic stir bar, 0.127 mmol of the corresponding o–iodoaryl cinnamate,

408   1.3 mL of dimethylacetamide, 0.2 mmol of KOAc or K_2CO_3 (these two bases gave

409   systematically the same results), 0.1 mmol of tetrapropylammonium bromide and $2 \cdot 10^{-3}$

410   mmol of palladium acetate (2 mol %) were added. The mixture was placed in a pre–heated oil

411   bath and magnetically stirred at 140 °C. Aliquots (50 µl) were periodically taken out, diluted

412   in a solution of the internal standard in dichloromethane, and analyzed by CG. After 20 h, the

413   reaction mixture was cooled, 4 mL of water were added and the mixture was extracted with 3

414   mL ethyl acetate (three times), washed with brine and dried over magnesium sulfate. Products

415   were purified by flash chromatography in a hexane: ethyl acetate (9:1) mixture as an eluent.

416   *N,N*–dimethylacetamide (DMAc) was used as a solvent instead of DMF since the latter starts

417   to decompose at temperatures ~140 ºC to give free dimethylamines and CO, which can

418   deactivate the clusters. Despite using a relatively high concentrated solution (0.1–0.5 M), the

419   intramolecular coupling proceeds well, since the intermolecular coupling of **1a(a)–m** does not

420   proceed at all in accordance with the steric hindrance associated to disubstituted alkenes.

421   Notice that non–dried *N*–alkyl amides are the solvents of choice here since they generate and

422   stabilize ultra–small catalytically active Pd species for the coupling. General bases for

423   Mizoroki–Heck couplings worked well, perhaps except amines, which typically show a better

424   performance, and the presence of halides (iodide and bromides) as ligands seem compatible

425   with the regio–irregular coupling, at least an initial ten–fold excess of bromide.

426   **α–Selective intermolecular coupling of aryl iodides and styrenes.** In a 5 mL vial equipped

427   with a magnetic stir bar and a reflux condenser, 0.1 mmol of the corresponding iodobenzene,

428   0.3 mmol of the corresponding styrene, 20 mol% of Pd–Cs(3)X and 3 mL of mesitylene (1M)

429   were added. The use of external bases, including Cs_2CO_3, or *n*–butyl acrylate as an alkene

430   partner, yields β–*E*–alkenes as the only products of the reaction.A higher amount of catalytic

431   Pd compared to the intramolecular coupling in solution must be employed, not only because

432   of the inherent difficulty of the intermolecular coupling, but also of the need of using a Pd–

433   embedded microporous solid catalysts (it is difficult at this point to know how catalytically

434   active Pd(0) is initially formed, although the fact that the electron-rich zeolite, i.e. Cs-X, is the

435   more active catalyst, suggest an electron donation from the zeolite to the Pd clusters during

436   reaction.) Thermal dehydration of the Pd–CsX is not recommended since Pd is prone to

437   reduce and agglomerate into Pd black. The reaction was then heated at 175 °C under reflux at

438   the open air. Aliquots of the supernatant (50 µl) were periodically taken out after stopping the

439   stirring for a few seconds, and diluted in a toluene solution with the internal standard, to be

440   analyzed by CG. After 2 h, the reaction mixture was cooled, 5 mL of water were added and

441   the mixture was extracted with 5 mL ethyl acetate (three times), washed with brine and dried

442   over magnesium sulfate. It was then purified by flash chromatography in a hexane: ethyl

443   acetate (4:1) mixture as an eluent. The kinetic radius of the different para–substituted

444   iodobenzenes was calculated on the basis of molecular mechanics (MM2) at minimized

445   energy and also on experimental X–ray distances. Substrate **1a** is not reactive with any Pd–

446   zeolite catalyst since it cannot diffuse into the zeolite pores.

447   **In–flow α–selective intermolecular coupling of iodobenzene 5a and styrene 6a.** A syringe

448   was charged with a mesitylene solution (38 ml) of iodobenzene **5a** (0.143 ml) and styrene **6a**

449   (0.42 ml), and the mixture was pumped at atmospheric pressure at a flow of 12.5 ml·h^{-1} on the

450   top of a tubular stainless steel (10 mm id), where a previously pelletized and sieved to a

451   particle size 0.4–0.5 mm Pd–Cs(2)X (2.4 g) was placed in. The reactor was filled with glass

452   wool, to favour the uniform distribution of the flow through the catalyst bed and to avoid

453   preferential pathways. The reaction temperature was maintained at 175 ^{o}C and the samples

454   were collected by gravity every 5 minutes. Known amounts of dodecane or o–xylene were

455   added as an external standard and the samples were analysed by GC. After the reaction was

456   completed, the reactivation of the catalyst was performed in situ by heating at 140 ^{o}C while

457   the reactor was fed with a solution of Cs_2CO_3 for 2 h at 0.5 ml·min^{-1}, and then dried at 25 ºC

458   with a N_2 stream.

459   **Photoredox catalysed coupling of aryl bromides with 1,1–diphenylethylenes by means of**

460   **TFU technology.** In a quartz cuvette (4 mL) with a magnetic stirring bar, an acetonitrile (2.6

461   mL) and dimethylacetamide (0.4 mL) solution of aryl halide (30 μmol, 0.01 M, 1.0 equiv.),

462   1,1–diphenylethylene (400 μmol, 0.1 M, 10 equiv.), **BOPHY** (100 μg, 0.3 μmol, 0.0001 M,

463   0.01 equiv.), **DPA** (1 mg, 3 μmol, 0.001 M, 0.1 equiv.) and 1–dodecanenitrile (6.5 μL, 0.01

464   M, 1 equiv.) as an internal standard, was prepared. The cuvette was sealed with a septum and

465 placed in a water–cooling holder to keep a constant temperature around 20 ºC. The mixture

466 was first purged with a nitrogen gas flux for 10 min, maintaining subsequently nitrogen

467 atmosphere during the photolysis. Then, irradiation of the reaction was performed for 5 h with

468 an external diode laser pointer (λ_{exc} = 445 nm ± 10) through one face of the cuvette. The

469 reaction progress was monitored by GC analysis. For isolation purposes, water (10 mL) was

470 added and the aqueous phase was extracted with ethyl acetate (3 × 10 mL). The combined

471 organic phases were washed with brine (10 mL), dried over magnesium sulphate, filtered

472 from the drying agent, and concentrated in vacuum. The crude product was purified by high

473 pressure liquid chromatography (HPLC), using acetonitrile : water (80:20 *v/v*) as an eluent.

474 **Transient absorption spectroscopy (TAS).** Measurements were carried out with a LP980–

475 KS Laser Flash Photolysis Spectrometer, and wavelength specific kinetic measurements are

476 made using photomultiplier and digital storage oscilloscope, while time gated spectral

477 measurements are obtained using an image intensified CCD camera. The pump source is a

478 Flashlamp pumped Q–switched Nd:YAG laser operating at 1064, 532, 355, 266 nm (INDI –

479 40–10–HG Quanta–Ray Spectra Physics). To select other excitation wavelength, an optical

480 parametric oscillator OPO (primoScan BB Spectra Physics) is pumped by the third Harmonic

481 (355 nm, pump energy = 120 mJ) of a Nd:YAG laser from Spectra Physics with typical pulse

482 duration of 0–3 ns. The wavelength is set from 250 nm to about 2750 nm, with a linewidth of

483 about 3.5–6 cm^{-1}, and the repetition rate was 10 Hz. The white probe light is generated by a

484 pulsed xenon flash lamp [150 W, ozone free (230–900 nm)] and passes the sample orthogonal

485 to the pump beam. The duration of the probe pulse is 250 μs, and the time resolution in each

486 window is about 20% of the temporal window width. The transient absorption spectra are

487 recorded by an ICCD camera (Andor DH320T–25F–03) with a 25 mm diameter and spectral

488 range of 180–850 nm.

489   **Computational.** DFT calculations were performed with the Gaussian09 software, using the

490   B3LYP functional in combination with the 6–311G** and LANL2DZ basis sets. The solvent

491   was not included in the calculations since it is involved in the Pd cluster generation[16,19] but

492   apparently not in the catalytic events, since the use of a pre–formed Pd_4 cluster within a metal

493   organic framework (MOF) solid[21] allowed to carry out the intramolecular coupling of **1a** in

494   toluene as well as DMF, with similar yields in both cases (Supplementary Figure 7).

495   Nevertheless, the aim of the DFT study was to support the structure of a potential active site

496   with geometric relations, however, the environment is much more complex (i.e. variation /

497   development of cluster sizes up to flat surfaces under heating, halides, other substrates and

498   additives) and dynamic, which must be taken in account.

499   **Synchrotron experiments.** X–ray absorption experiments, at the Pd (24350 eV) K–edge,

500   were performed at the BL22 (CLÆSS) beamline of ALBA synchrotron (Cerdanyolla del

501   Vallès, Spain). The white beam was monochromatized using a Si (311) double crystal cooled

502   by liquid nitrogen; harmonic rejection was performed using Rh–coated silicon mirrors. The

503   spectra were collected in transmission mode. Reference patterns (e.g. metal foil) were

504   measured simultaneously between I1 and I2 and used for spectra alignment. To identify the

505   location of Pd clusters in Pd–Cs(3)X, we have employed a combination of high–resolution

506   high–angle annular dark-field scanning transmission electron microscopy (HR HAADF–

507   STEM) and integrated differential phase contrast (iDPC) imaging techniques to

508   simultaneously visualize both Pd clusters and the zeolite structure with atomic resolution,

509   respectively, under low–dose conditions[32,33]. As shown in Figure 4c, some bright dots can be

510   clearly identified in the HR HAADF–STEM images recorded at off–axis orientation together

511   with some larger nanoparticles. Although the vast majority of the zeolite crystals analyzed in

512   this study were off–axis STEM images, the visualization of the tiny Pd entities is improved

513   due to the reduction of electron channeling effects[34], and considering the image simulation

514   results, the bright dots appearing in the HR HAADF-STEM images can be ascribed to Pd

515   clusters (Supplementary Figure 8). The position of the Pd clusters can be determined to be

516   within the zeolite channels by correlating the bright dots in the corresponding iDPC image.

517   **Microscopy experiments.** Samples for electron microscopy studies were prepared by

518   dropping the suspension of the solid samples in DMF directly onto holey–carbon–coated

519   copper grids. For Pd–containing base zeolite, powder sample were embedded in an epoxy

520   resin and sliced at a thickness of less than 100 nm with an ultramicrotome. They were then

521   deposited on holey carbon copper grid before TEM observation. HR HAADF–STEM and

522   STEM–iDPC studies were performed on a double–aberration–corrected, monochromated, FEI

523   Titan^3 Themis 60–300 microscope working at 300 kV.

Data availability

525   The datasets generated during and/or analysed during the current study are included in this

526   published article (and its supplementary information files) or available from the

527   corresponding author on reasonable request. If possible, datasets will be also deposited in

528   public repositories of the UPV and CSIC.

529

REFERENCES

531   1. Wu X.–F., Anbarasan P., Neumann H. & Beller M. From noble metal to nobel prize:

532   palladium–catalysed coupling reactions as key methods in organic synthesis. *Angew. Chem.*

533   *Int. Ed.* **49**, 9047–9050 (2010).

534   2. Beletskaya I. P. & Cheprakov A. V. The Heck reaction as a sharpening stone of palladium

535   catalysis. *Chem. Rev.* **100**, 8, 3009–3066 (2000).

536   3. Phan N. T. S., Van Der Sluys M., & Jones C. W. On the nature of the active species in

537   palladium catalysed Mizoroki–Heck and Suzuki–Miyaura couplings – homogeneous or

538   heterogeneous catalysis, a critical review. *Adv. Synth. Catal.* **348**, 609–679 (2006).

539   4. Mo J. & Xiao J. The Heck reaction of electron–rich olefins with regiocontrol by hydrogen–

540   bond donors. *Angew. Chem. Int. Ed.* **45**, 4152 –4157 (2006).

541   5. Wucher P. et al.Breaking the regioselectivity rule for acrylate insertion in the Mizoroki–

542   Heck reaction. *PNAS* **108**, 22, 8955–8959 (2011).

543   6. Barluenga, J., Moriel, P., Valdés, C. & Aznar, F. N. Tosylhydrazones as reagents for cross–

544   coupling reactions: a route to polysubstituted olefins. *Angew. Chem. Int. Ed.* **46**, 5587−5590

545   (2007).

546   7. Zou Y. et al. Selective arylation and vinylation at the α position of vinylarenes. *Chem. Eur.*

547   *J.* **19**, 3504–3511 (2013).

548   8. Tang J., Hackenberger D. & Goossen L. J. Branched arylalkenes from cinnamates:

549   selectivity inversion in heck reactions by carboxylates as deciduous directing groups. *Angew.*

550   *Chem. Int. Ed.* **55**, 11296–11299 (2016).

551   9. Sullivan R. J., Freure G. P. R. & Newman S. G. Overcoming scope limitations in cross–

552   coupling of diazo nucleophiles by manipulating catalyst speciation and using flow diazo

553   generation. *ACS Catal.* **9**, 6, 5623–5630 (2019).

554   10. Nakashima Y., Hirata G., Sheppard T. D. & Nishikata T. The Mizoroki–Heck reaction

555   with internal olefins: reactivities and stereoselectivities. *Asian J. Org. Chem.* **9**, 480–491

556   (2020).

557   11. Torborg C. & Beller M. Recent applications of palladium–catalysed coupling reactions in

558   the pharmaceutical, agrochemical, and fine chemical industries. *Adv. Synth. Catal.* **351**, 3027–

559   3043 (2009).

560   12. Dounay A. B. & L. E. Overman. The asymmetric intramolecular Heck reaction in natural

561   product total synthesis. *Chem. Rev.* **103**, 2945–2963 (2003).

562   13. Tsvelikhovsky D. & Buchwald S. L. Synthesis of heterocycles via Pd–ligand controlled

563   cyclization of 2–chloro–n–(2–vinyl)aniline: preparation of carbazoles, indoles,

564   dibenzazepines, and acridines. *J. Am. Chem. Soc.* **132**, 14048–14051 (2010).

565   14. Weng S.–S., Ke C.–S., Chen F.–K., Lyu Y.–F. & Lin G.–Y. Transesterification catalysed

566   by iron(III) β–diketonate species. *Tetrahedron* **67**, 1640–1648 (2011).

567   15. Nájera C. Oxime–derived palladacycles: applications in catalysis. *ChemCatChem* **8**,

568   1865–1881 (2016).

569   16. Leyva–Pérez A., Oliver–Meseguer J., Rubio–Marqués P. & Corma A. Water–stabilized

570   three– and four–atom palladium clusters as highly active catalytic species in ligand–free C–C

571   cross–coupling reactions. *Angew. Chem. Int. Ed.* **52**, 11554 –11559 (2013).

572   17. Zhu F., Li Y., Wang Z. & Wu X.–F. Iridium–catalysed carbonylative synthesis of

573   chromenones from simple phenols and internal alkynes at atmospheric pressure. *Angew.*

574   *Chem. Int. Ed.* **55**, 14151–14154 (2016).

575   18. Li X. et al. Palladium–catalysed enantioselective intramolecular dearomative Heck

576   reaction. *J. Am. Chem. Soc.* **140**, 13945−13951 (2018).

577   19. Fernández E. et al. Base–controlled Heck, Suzuki, and Sonogashira reactions catalysed by

578   ligand–free platinum or palladium single atom and sub–nanometer clusters. *J. Am. Chem. Soc.*

579   **141**, 1928−1940 (2019).

580   20. Sperger T., Stirner C. K., Schoenebeck F. Bench-stable and recoverable palladium(I)

581   dimer as an efficient catalyst for Heck cross-coupling. *Synth.* **49**, 1, 115–120 (2017).

582   21. Fortea–Pérez F. R. et al. The MOF–driven synthesis of supported palladium clusters with

583   catalytic activity for carbene–mediated chemistry. *Nat. Mater.* **16**, 760–766 (2017).

584   22. von Schenck H., Åkermark B. & Svensson M. Electronic control of the regiochemistry in

585   the Heck reaction. *J. Am. Chem. Soc.* **125**, 3503–3508 (2003).

586   23. Deeth R. J., Smith A. & Brown J. M. Electronic control of the regiochemistry in

587   palladium–phosphine catalysed intermolecular Heck reactions. *J. Am. Chem. Soc.* **126**, 7144–

588   7151 (2004).

589   24. Djakovitch L. & Koehler K. Heck reaction catalysed by Pd–modified zeolites. *J. Am.*

590   *Chem. Soc.* **123**, 5990–5999 (2001).

591   25. Dams M. et al. Pd–zeolites as heterogeneous catalysts in Heck chemistry, *J. Catal.* **209**,

592   225–236 (2002).

593   26. –Marqués P., Rivero–Crespo M. A., Leyva–Pérez A. & Corma A. Well–defined noble

594   metal single sites in zeolites as an alternative to catalysis by insoluble metal salts. *J. Am.*

595   *Chem. Soc.* **137**, 11832−11837 (2015).

596   27. Corma A., García H., Leyva A. & Primo A. Basic zeolites containing palladium as

597   bifunctional heterogeneous catalysts for the Heck reaction. *Appl. Catal. A–Gen.* **247**, 41–49

598   (2003).

599   28. Sun, T., Seff, K., Heo, N. H. & Petranovskii, V. P. A cationic cesium continuum in zeolite

600   X. *Science* **259**, 495–497 (1993).

601   29. Agostini G. et al.Preparation of supported Pd catalysts: from the Pd precursor solution to

602   the deposited Pd^{2+} phase. *Langmuir*, **26**, 13, 11204–11211 (2010).

603   30. Cerrillo J. L. et al.Nature and evolution of Pd catalysts supported on activated carbon

604   fibers during the catalytic reduction of bromate in water. *Catal. Sc. Tech.* **10**, 13, 3646–3653

605   (2020).

606   31. Liu L. & Corma A. Metal catalysts for heterogeneous catalysis: From single atoms to

607   nanoclusters and nanoparticles. *Chem. Rev.* **118**, 10, 4981–5079 (2018).

608   32. Liu L., Lopez–Haro M., Lopes C. W., Li C., Concepcion P., Simonelli L., Calvino J. J. &

609   Corma, A. Regioselective generation and reactivity control of subnanometric platinum

610   clusters in zeolites for high–temperature catalysis. *Nat. Mater.* **18**, 8, 866–873 (2019).

611   33. Liu L. et al.Structural modulation and direct measurement of subnanometric bimetallic

612   PtSn clusters confined in zeolites. *Nat. Catal.* **3**, 8, 628–638 (2020).

613   34. Liu, L. et al. Tutorial: structural characterization of isolated metal atoms and

614   subnanometric metal clusters in zeolites. Nat Protoc (2020). https://doi.org/10.1038/s41596-

615   020-0366-9

616   35. Li P. et al.Explaining the influence of the introduced base sites into alkali oxide modified

617   CsX towards side–chain alkylation of toluene with methanol. *RSC Adv.* **9**, 13234–13242

618   (2019).

619   36. Concepcion–Heydorn P. et al.Structural and catalytic properties of sodium and cesium

620   exchanged X and Y zeolites, and germanium substituted X zeolite. *J. Mol. Catal. A* **162**, 227–

621   246 (2000).

622   37. Seo D.–W., Rahma S. T., Reddy B. M. & Parka S.–E. Carbon dioxide assisted toluene

623   side–chain alkylation with methanol over Cs–X zeolite catalyst. *J. CO_2 Util.* **26**, 254–261

624   (2018).

625   38. Rivero Crespo M. Á. et al. Intermolecular carbonyl–olefin metathesis with vinyl ethers

626   catalysed by homogeneous and solid acids in flow. *Angew. Chem. Int. Ed.* **59**, 3846–3849

627   (2020).

628   39. Kashani S. K., Jessiman J. E. & Newman S. G. Exploring homogeneous conditions for

629   mild Buchwald–Hartwig amination in batch and flow. *Org. Process Res. Dev.* (2020).

630   doi.org/10.1021/acs.oprd.0c00018.

631   40. Alami M., Liron F., Gervais M., Peyrat J.–F. & Brion J.–D. Ortho substituents direct

632   regioselective addition of tributyltin hydride to unsymmetrical diaryl (or heteroaryl) alkynes:

633   an efficient route to stannylated stilbene derivatives. *Angew. Chem. Int. Ed.* **41**, 1578–1580

634   (2002).

635   41. Onuigbo L., Raviola C., Di Fonzo A., Protti S. & Fagnoni M. Sunlight–driven synthesis

636   of triarylethylenes (TAEs) via metal–free Mizoroki–Heck–type coupling. *Eur. J. Org. Chem.*

637   **38**, 5297–5303 (2018).

638   42. Wang H., Gao Y., Zhou C. & Li G. Visible–light–driven reductive carboarylation of

639   styrenes with CO_2 and aryl halides. *J. Am. Chem. Soc.* **142**, 8122−8129 (2020).

640   43. Zuo Z. & MacMillan D. W. C. Decarboxylative arylation of α–amino acids via

641   photoredox catalysis: a one–step conversion of biomass to drug pharmacophore. *J. Am. Chem.*

642   *Soc.* **136**, 14, 5257–5260 (2014).

643   44. Bardagi J. I., Ghosh I., Schmalzbauer M., Ghosh T. & König B. Anthraquinones as

644   photoredox catalysts for the reductive activation of aryl halides. *Eur. J. Org. Chem.* **1**, 34–40

645   (2018).

646   45. Majek M., Faltermeier U., Dick B., Pérez–Ruiz R., Jacobi von Wangelin, A. Application

647   of visible–to–UV photon upconversion to photoredox catalysis: the activation of aryl

648   bromides. *Chem. Eur. J.* **21**, 15496−15501 (2015).

649   46. López–Calixto C. G., Liras M., de la Peña O'Shea V. A., Pérez–Ruiz, R. Synchronized

650   biphotonic process triggering C–C coupling catalytic reactions. *Appl. Catal. B* **237**, 18−23

651   (2018).

652   47. Martínez–Gualda A. M. et al. Chromoselective access to *Z*– or *E*–allylated amines and

653   heterocycles by a photocatalytic allylation reaction. *Nat. Commun.* **10**, 2634 (2019).

654   48. Yang J., Liu J., Neumann H., Franke R., Jackstell R. & Beller M. Direct synthesis of

655   adipic acid esters via palladium catalysed carbonylation of 1,3–dienes. *Science* **366**, 1514–

656   1517 (2019).

657   49. Uehling M. R., King R. P., Krska S. W., Cernak T. & Buchwald S. L. Pharmaceutical

658   diversification via palladium oxidative addition complexes. *Science* **363**, 405–408 (2019).

659   50. Ross S. P., Rahman A. A. & Sigman M. S. Development and mechanistic interrogation of

660   interrupted chain–walking in the enantioselective relay Heck reaction. *J. Am. Chem. Soc*. **142**,

661   23, 10516–10525 (2020).

662   **Acknowledgements**

672   **Author contributions**

673   Author contributions are as follows: F. G.–P. performed the synthesis and characterization of

674   Pd catalysts and the corresponding reactions, R. G. carried out and interpreted the

675   computational studies, J. O.–M. performed and interpreted the synchrotron studies and the in–

676   flow reactions, R. P.–R. and M. C. J. designed and supervised the investigations on

677   photoredox catalysed coupling between aryl bromides and 1,1–diphenylethylenes, M. L.–H.

678   and J. C. H.–G. carried out and interpreted HR STEM measurements, image analysis and

679   simulations, M. B. carried out and supervised the computational studies, J. C.–S and R. P.–R.

680   performed the photoredox catalysed reactions together with the isolation, purification and

681   characterization of TAEs, and A. L.–P. performed the synthesis and characterization of Pd

682   catalysts and the corresponding reactions, supervised the whole study and wrote the

683   manuscript (all authors also contributed to the latter).

684   **Competing interests**

685   The authors declare that they have no competing interests.

686

FIGURE LEGENDS

688 **FIGURE 1 Expanding the chemical space of the Mizoroki–Heck reaction.** a) The

689 Mizoroki–Heck coupling and the two possible regioselective products α and β. EWG:

690 Electron–withdrawing group. EDG: Electron–donor group. b) Mechanistic rationale for the

691 formation of the α and β products, and the proposal here presented. c) Spatially hindered

692 coupling in polysubstituted alkenes, and the proposal here presented. d) Schematic illustration

693 of the Mizoroki–Heck chemical space, with the yet unachieved couplings. e) The three

694 strategies studied here to significantly expand the chemical space of the Mizoroki–Heck

695 reaction: 1) the Pd cluster–catalysed α–selective intramolecular coupling of iodoaryl

696 cinnamates, 2) the Pd–zeolite–catalysed α–selective intermolecular coupling of aryl iodides

697 with styrenes, and 3) the organophotocatalysed coupling of aryl bromides with polysubstitued

698 ethylenes under visible light.

699 **TABLE 1 Catalytic results for the α–selective intramolecular coupling.** Catalytic results

700 for the intramolecular coupling of **1a** with different soluble Pd catalysts and under different

701 reaction conditions. B) Scope of the reaction with Pd_{3-4} clusters as a catalyst, under optimized

702 reaction conditions.

703 **FIGURE 2 Scope for the α–selective intramolecular coupling.** Scope of the reaction with

704 Pd_{3-4} clusters as a catalyst, under optimized reaction conditions.

705 **FIGURE 3 DFT calculations of the α–selective intramolecular coupling.** a) Most stable

706 adsorption modes of of **1a** on Pd_4 clusters, b) LUMO orbital of Pd_3 and Pd_4, c) optimized

707 geometries of transition states and products for the α– and β–intramolecular coupling, and d)

708 corresponding energy profile. In parenthesis, relative energies with respect to the most stable

709 structure A (in $kcal \cdot mol^{-1}$). Color atom scheme: Pd in blue, I in pink, C in grey, O in red, and

710 H in white. e) Visualization of the Pd clusters in solution by means of high–resolution high–

711   angle annular dark–field scanning transmission electron microscopy (HR HAADF–STEM),

712   with the corresponding histogram in the range 0–2 nm.

713   **FIGURE 4 Pd–containing base zeolites for the α–selective intermolecular coupling.** a)

714   Catalytic design. b) FT of the k3–weighted phase–uncorrected χ(k) functions and Normalized

715   XANES spectra. c) Top row: large-area and detailed HR HAADF-STEM image and the iDPC

716   image of the same area for a Pd–Cs(3)X sample. In the HAADF–STEM image, the

717   identification of Pd entities are clearly imaged due to the higher contrast. In the corresponding

718   iDPC image, the atomic structure of the zeolite Cs(3)X is also clearly revealed. Bottom row:

719   precise location of sub–nanometer (<1 nm) Pd clusters within the zeolite Cs(3)X framework,

720   by combining the images obtained in the two modes.

721   **TABLE 2 Catalytic results of Pd–containing base zeolites.** Catalytic results for the

722   intermolecular coupling between iodobenzene **5a** and styrene **6a** with different Pd–supported

723   base zeolites.

724   **FIGURE 5 Steric effects and reaction in–flow.** a) Correlation of the reactivity and

725   selectivity with the size of the iodobenzene coupling partner, when using Pd–Cs(3)X as a

726   catalyst under optimized reaction conditions. b) In–flow reaction: intermolecular coupling of

727   **5a** with **6a** in a fixed–bed reactor containing 0.5 mm pellets of Pd–Cs(3)X. Error bars account

728   for a 5% uncertainity and were calculated by standard deviations with the Excel[TM] software.

729   **FIGURE 6 Scope for the α–selective intermolecular coupling.** Results for different

730   iodobenzenes and alkenes under optimized reaction conditions.

731   **EXTENDED DATA FIGURE 1 Scope for the coupling of aryl bromides with**

732   **polysubstituted ethylenes by means of TFU photoredox catalysis.** Examples of Mizoroki–

733   Heck couplings between aryl bromides and polysubstituted alkenes using TFU technology.

734   Reaction conditions: aryl bromide (10^{-2} M), polysubstituted alkenes (0.1 M), **BOPHY** (10^{-4}

735 M) and **DPA** (10^{-3} M), 3 ml of ACN/DMA 5/1 *v/v* using a blue laser pointer (445 nm ± 10)

736 under nitrogen atmosphere during 5 h. [i] This reaction was carried out using 2–acetyl–5–

737 chlorothiophene.

738 **EXTENDED DATA FIGURE 2 Mechanism of the TFU photoredox catalysed Heck**

739 **coupling of polysubstituted ethylenes.** a) Transient absorption spectra of **BOPHY** (0.001

740 mM) and **DPA** (1 mM) in N_2 ACN/DMA (5/1 *v/v*) solution (λ_{exc} = 485 nm). b) Proposed

741 photocatalytic mechanism of the Mizoroki–Heck coupling reaction between aryl bromides

742 and polysubstituted alkenes. Cascade processes involving: ISC (intersystem crossing), TTEnT

743 (triplet–triplet energy transfer), TFU (triplet fusion upconversion), SET (single electron

744 transfer), C–C bond formation and BET (back electron transfer). c) Delayed emission spectra

745 of a mixture of **BOPHY** (0.1 mM) and **DPA** (1 mM) in bubbled (N_2) ACN/DMA (5/1 *v/v*)

746 after excitation (485 nm) with a pulsed laser in the absence (black) and in the presence of 4–

747 bromoacetophenone (10 mM). d) Transient absorption spectrum recorded at 2 μs after the

748 laser pulse of **BOPHY** (10^{-4} M) and **DPA** (10^{-3} M) in the presence of 4–bromoacetophenone

749 (10^{-2} M) and 1,1–diphenylethylene (0.1 M) in 3 ml of N_2 ACN/DMA (5/1 *v/v*); inset: decay

750 kinetic monitored at 500 nm after 485 nm TAS.

751

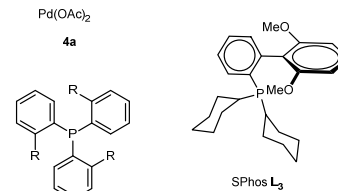752 **FIGURE 1 Expanding the chemical space of the Mizoroki–Heck reaction.**
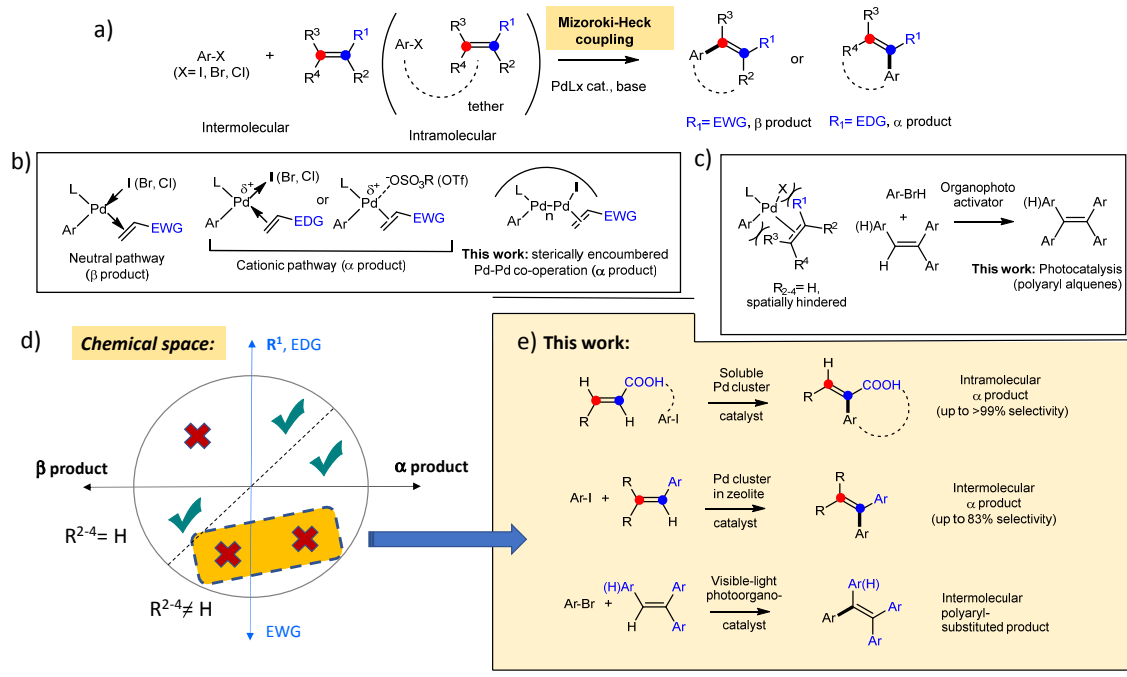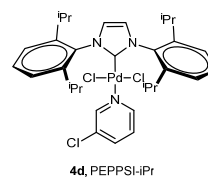

753

754

755

756 **TABLE 1 Catalytic results for the α–selective intramolecular coupling.**
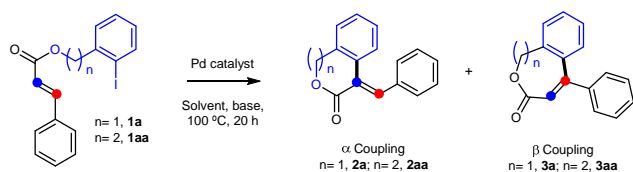
Entry	1	Catalyst	Solvent	Base	2 (%)[a]
1	1a	4a	Toluene	Cy_2NMe	-
2		$Pd(L1)_4$			-
3		$PdCl_2(L1)_2$			-
4		$PdCl_2(L2)_2$			9
5		4a-L3			4
6		4b			11
7		4c			14
8		4d			4
9[b]		4b			18
10[b]				K_2CO_3	17
11[b]			Water	Cy_2NMe	11
12[b]				K_2CO_3	9
13[c]			o-Xylene	KOAc	17
14[c]				K_2CO_3	16
15[c]				K_3PO_4	14
16[b,d]		Pd_{3-4}	DMF	Cy_2NMe	25
17[b]				K_2CO_3	30
18[b,c,d]					61
19[b,c,d]				**KOAc**	**63 (52)**
20[b,c,d]				K_3PO_4	62
21[b,c,d]	1aa			**KOAc**	**60 (55)**
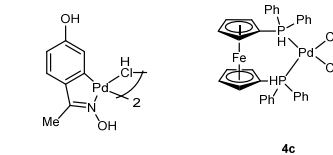
[a] GC yields, isolated yields between parentheses. **2/3** ratio was typically >5:1 for **1a** and >20:1 for **1aa**.
[b] With tetrapropylammonum bromide (TPABr, 20 mol%).
[c] 130 ºC. [d] Pd_{3-4} clusters generated in-situ from **4a** or **4b**.

757

758

34

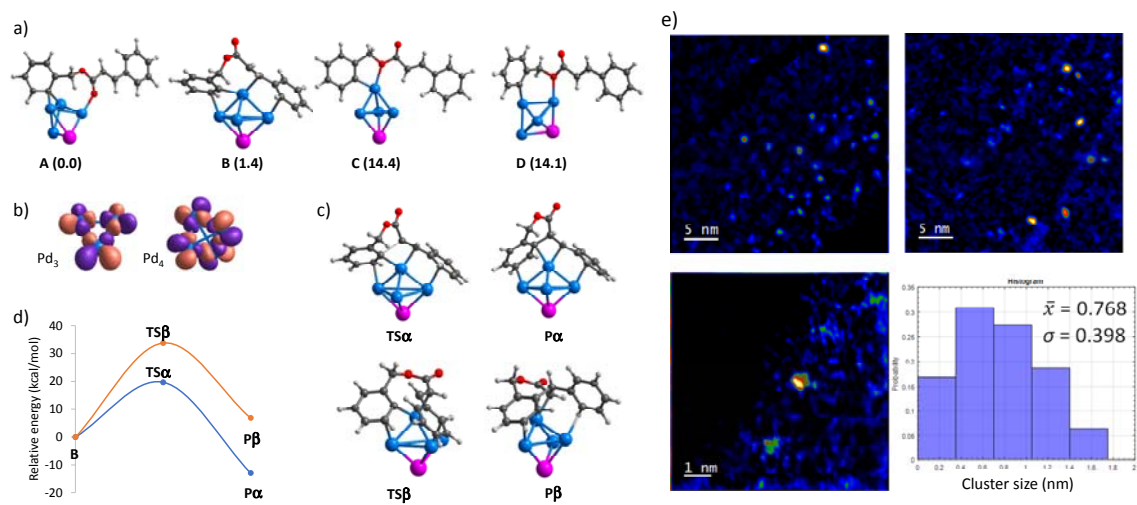759   **FIGURE 2 Scope for the α–selective intramolecular coupling.**

762
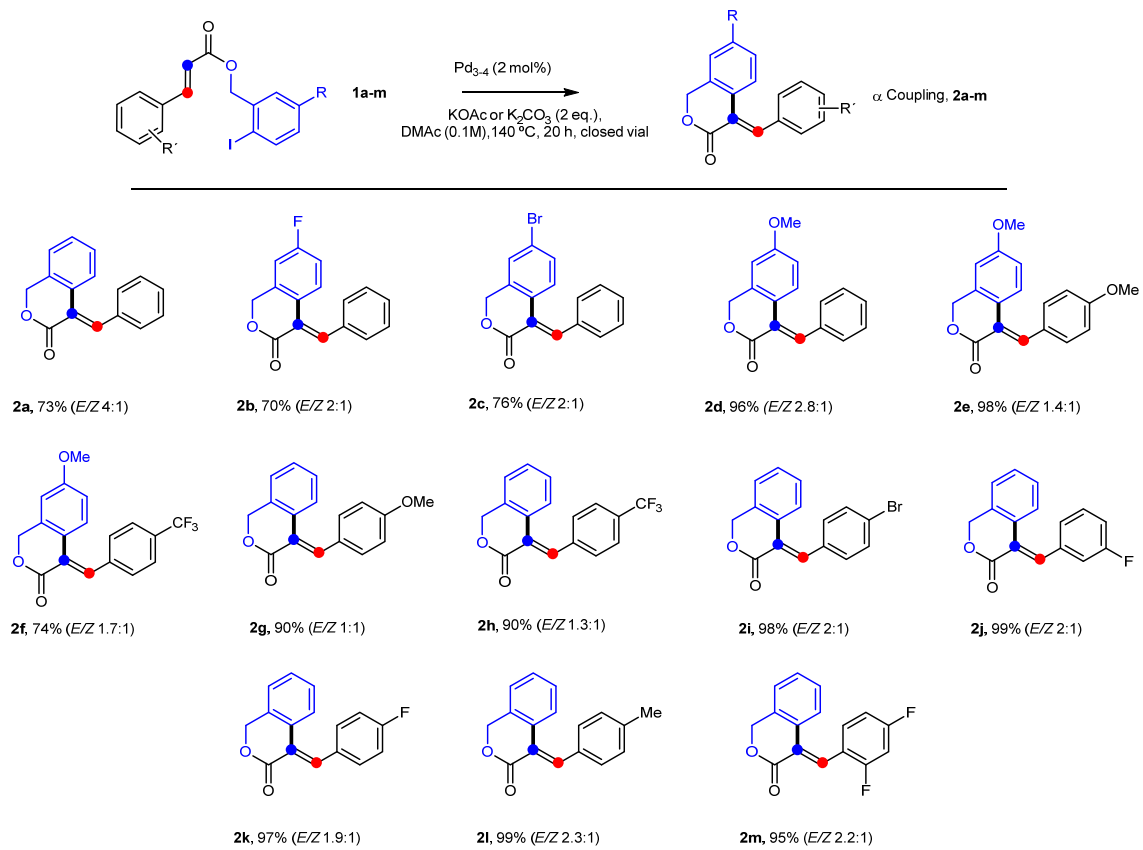
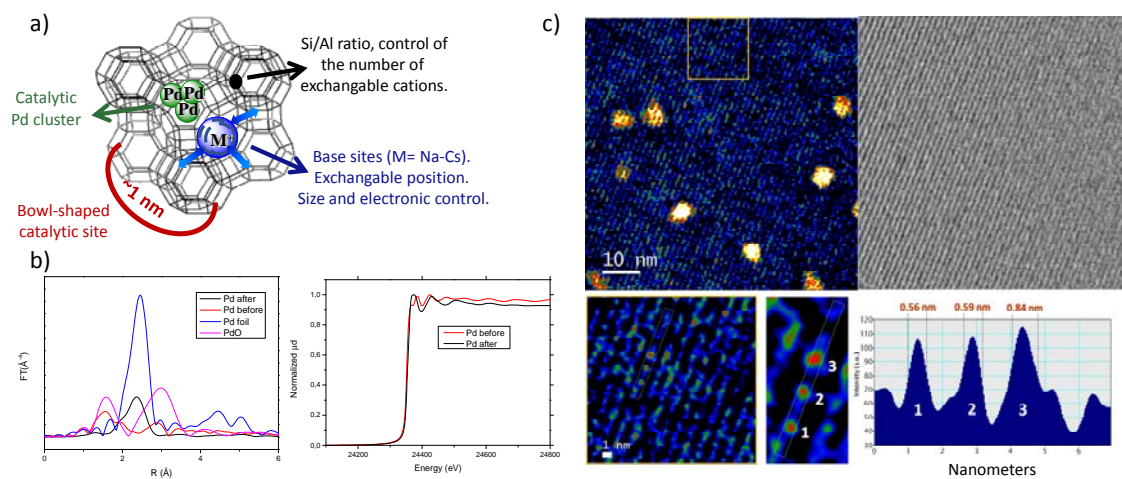**FIGURE 3 DFT calculations of the α–selective intramolecular coupling.**
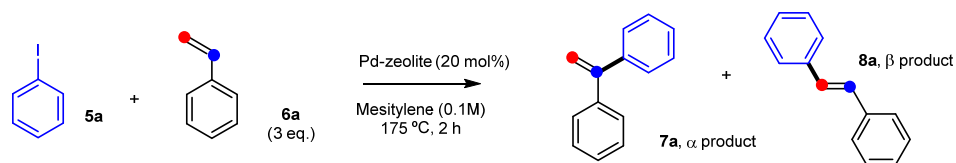

764

765

766

767   **FIGURE 4 Pd–containing base zeolites for the α–selective intermolecular coupling.**

768

769

770   **TABLE 2 Catalytic results of Pd–containing base zeolites.**

Entry	Catalyst	7a/8a (%)^a	Entry	Catalyst	7a/8a (%)^a
1	Pd^{2+}-NaY	- / -	11	Pd^{2+}-K(1)X	1 / 8
2	Pd-NaY	- / -	12	Pd-K(1)X	1 / 12
3	Pd^{2+}-K(1)Y	- / -	13	Pd-K(3)X	4 / 18
4	Pd-K(1)Y	- / -	14	Pd-Cs(1)X	22 / 75
5	Pd^{2+}-K(3)Y	- / -	15	Pd-Cs(2)X	37 / 62
6	Pd-K(3)Y	- / -	**16**	**Pd-Cs(3)X**	**64 (57) / 35**
7	Pd-Cs(1)Y	- / -	**17^b**	**Pd-Cs(3)X**	**73 (70) / 26**
8	Pd-Cs(3)Y	- / -	18^c	Pd-Cs(3)X	45 / 37
9	Pd^{2+}-NaX	- / -	19^d	Pd-Cs(3)X	47 / 53
10	Pd-NaX	- / -	20^e	Pd-Cs(3)X	46/17 [57/24]

^{a} GC yields, isolated yields between parentheses. ^{b} 5 wt% of Pd on the solid. ^{c} Non exchanged Cs sites added onto the solid. ^{d} Hierarchical zeolite. ^{e} CsI (1 eq.) in the solid; in brackets, the results after water washing and reuse.
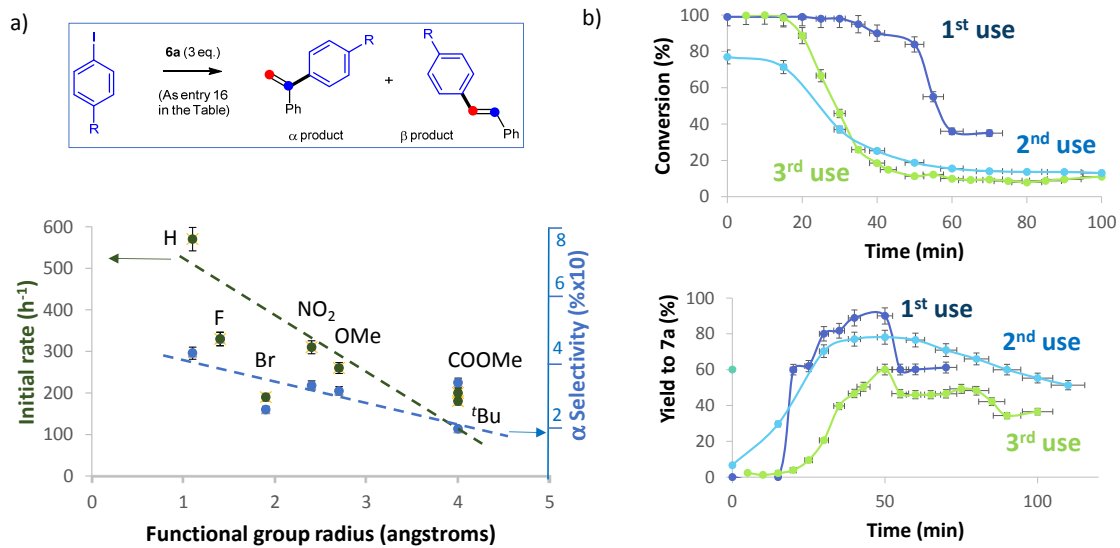
771

772
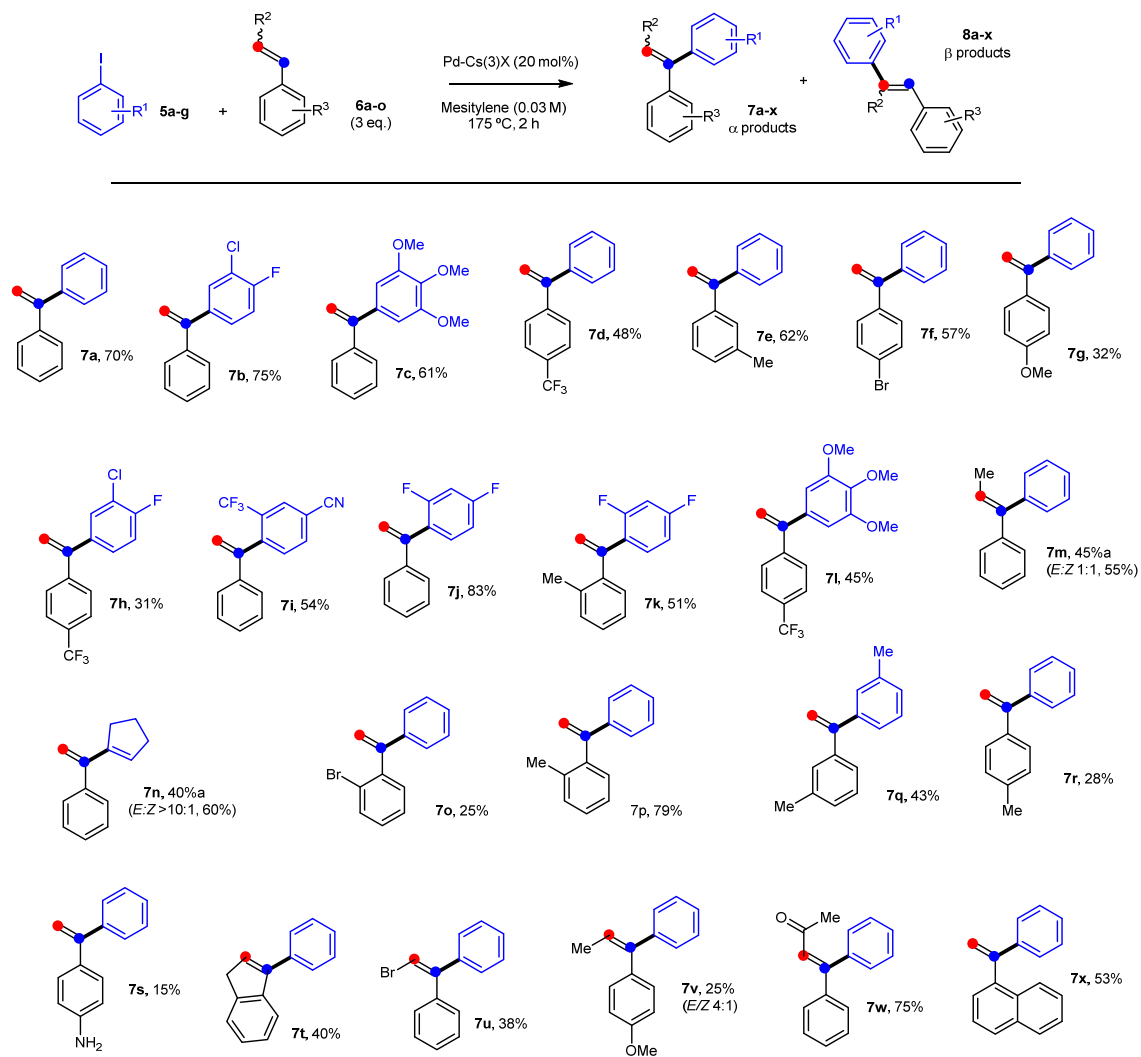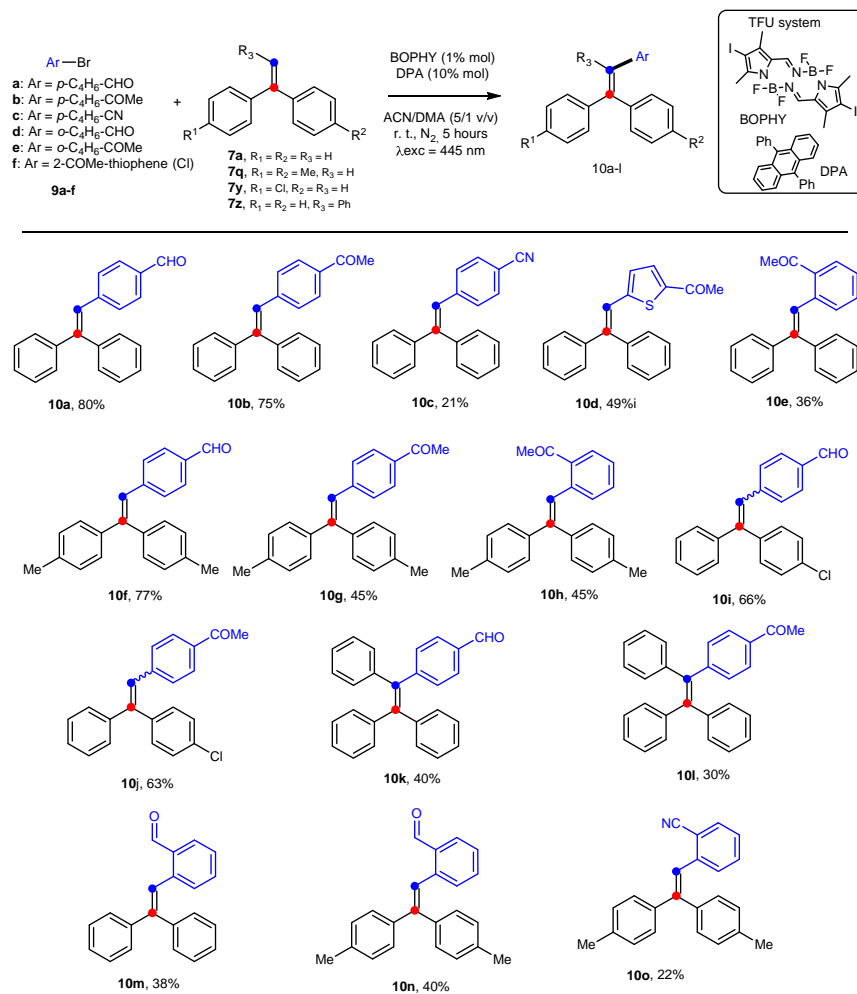
773

774

FIGURE 5 Steric effects and reaction in–flow.

FIGURE 6 Scope for the α–selective intermolecular coupling.
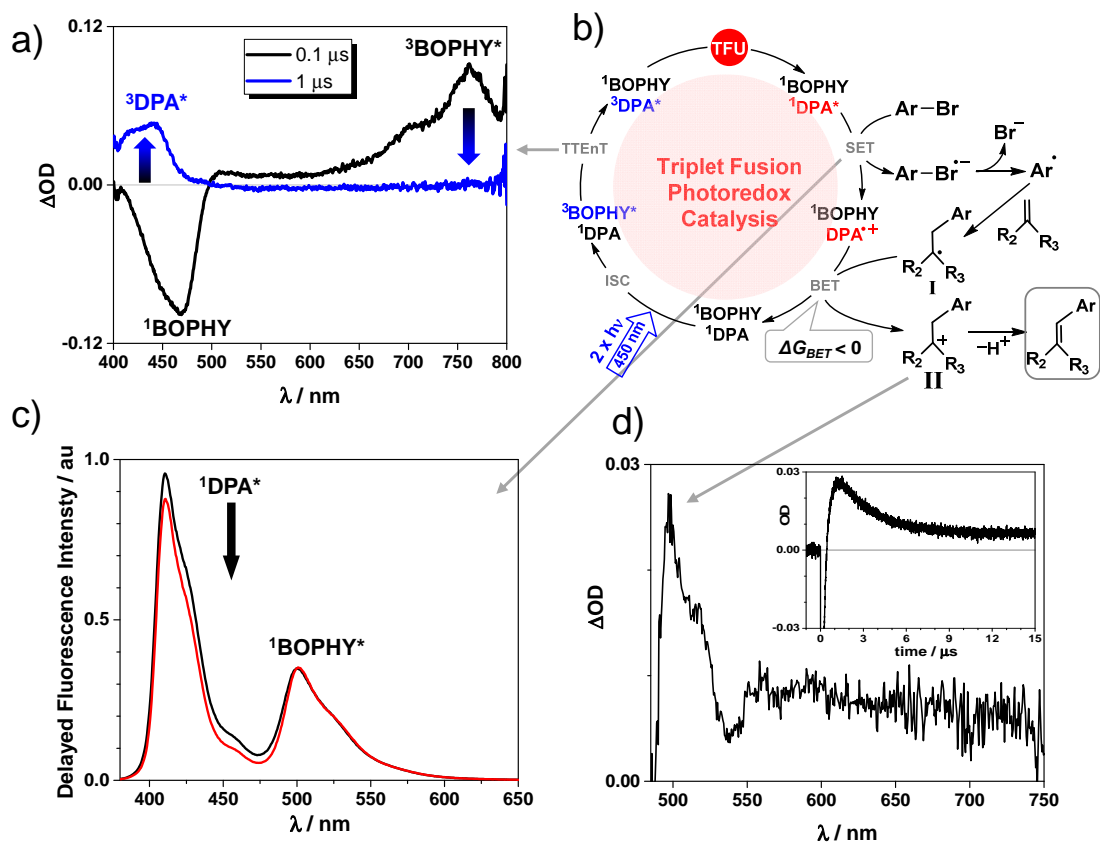
782 **EXTENDED DATA FIGURE 1 Scope for the coupling of aryl bromides with**

783 **polysubstituted ethylenes by means of TFU photoredox catalysis.**

784

785

EXTENDED DATA FIGURE 2 Mechanism of the TFU photoredox catalysed Heck

coupling of polysubstituted ethylenes.

788